PAPER Special Section on Emerging Technologies on Ambient Sensor Networks toward Future Generation

Two-Dimensional Imaging of a Pedestrian Using Multiple Wideband Doppler Interferometers with Clustering-Based Echo Association

Takuya SAKAMOTO[†,††a)], **Hiroki YAMAZAKI**[††], ***Members***, ***and*** **Toru SATO**[††], ***Fellow***

SUMMARY This paper presents a method of imaging a two-dimensional section of a walking person using multiple Doppler radar systems. Although each simple radar system consists of only two receivers, different radial speeds allow target positions to be separated and located. The signal received using each antenna is processed employing time–frequency analysis, which separates targets in the time–range–velocity space. This process is followed by a direction-of-arrival estimation employing interferometry. The data obtained using the multiple radar systems are integrated using a clustering algorithm and a target-tracking algorithm. Through realistic simulations, we demonstrate the remarkable performance of the proposed imaging method in generating a clear outline image of a human target in unknown motion.

key words: *radar imaging, Doppler radar, target velocity, human body*

1. Introduction

The automatic monitoring of people has a wide range of applications including home health care and safety monitoring of workers in harsh environments [1], [2]. An ultra-wideband (UWB) radar system has remarkable potential for the robust and reliable monitoring of people, because such systems, unlike optical cameras, can work in adverse environments such as dark, dusty and smoky locations with high humidity [3]–[6]. In addition, radar imaging does not obtain any information of texture, thus avoiding privacy concerns.

The ProVision 2 (L-3 Communications, NY) body scanner, which is one of the commercialized radar imaging systems deployed in many airports, uses approximately 320 receivers, and is too costly to be used at home. The applications assumed in this paper require a simple and cost-effective radar imaging system with a small number of receivers. Lin and Ling [7], [8] developed a Doppler interferometry imaging system that uses only three receivers. They separate multiple targets in the frequency domain using their different radial speeds, which is followed by direction-of-arrival (DOA) estimation using the phase difference between receivers. Their system uses continuous waves (CWs) and thus cannot resolve two targets with the same radial speed even if they are located apart in the range direction, which deteriorates the image quality.

To overcome the above difficulty, Saho et al. [9] applied the same concept to a UWB radar, so that targets are separated by their range and radial speed. They successfully demonstrated the imaging of a walking person using a 26-GHz radar system. The resultant image obtained using the method is, however, only a snapshot, in which only part of the human target is imaged, because radar signals are not reflected by the whole body at each moment. Therefore, it is indispensable to use echoes received over multiple snapshots; the images obtained over multiple snapshots are integrated to form a whole image of the target by compensating for the target velocity. Such an imaging method using velocity compensation has been reported in [10], but is only applicable to simple targets. The greatest challenge in this processing is the estimation of the velocity vector of each point in the image, where their radial speeds alone are not sufficient.

This study employs a UWB radar with two transmitters and four receivers that are placed in an indoor environment. The multipath effects are exploited to generate a two-dimensional (2D) sectional shape of the target. To form a radar image, it is necessary to compensate for the motion of targets, which requires the estimation of the target velocity vector. Each radar system, however, can only measure a radial speed. We need to combine the radial speeds measured using multiple receivers to estimate the velocity vector. It is thus crucial to associate echoes received using different receivers, which is not an easy task. In this paper, we propose a clustering-based algorithm to solve simultaneous equations imposed on target velocity vectors, which also enables association of echoes at the same time. The performance of the proposed method is demonstrated by applying it to simulation data, assuming a person walking in a narrow passage.

2. System Model

For simplicity, we consider a 2D problem with three targets, which are horizontal sections of the torso and arms of the target person. In an actual scenario, this model corresponds to the use of antennas that are horizontally omni-directional and vertically directive producing a horizontal fan beam. Figure 1 shows the top view of the 2D section of a human body and its motion assumed in this study. The torso

Manuscript received January 8, 2015.
Manuscript revised March 11, 2015.

[†]The author is with the Graduate School of Engineering, University of Hyogo, Himeji-shi, 671-2280 Japan.
[††]The authors are with the Graduate School of Informatics, Kyoto University, Kyoto-shi, 606-8501 Japan.
a) E-mail: t-sakamo@i.kyoto-u.ac.jp

DOI: 10.1587/transcom.E98.B.1795

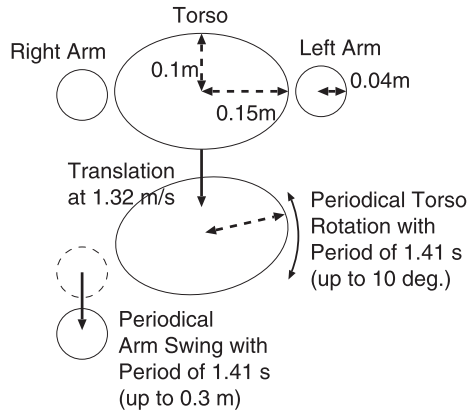

Fig. 1 Human body model used in our study. The whole body moves along a straight line while the torso rotates periodically, and arms swing synchronized with the torso rotation.

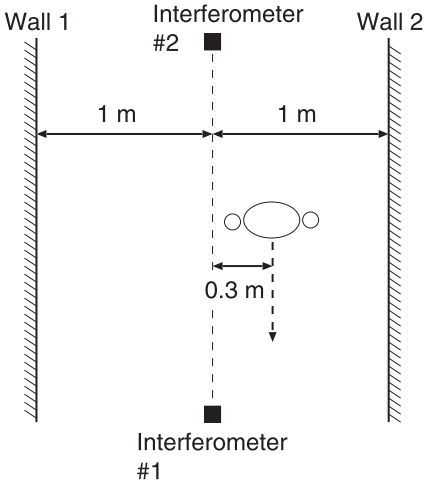

Fig. 2 Indoor scenario assumed in this study, where a person walking along a corridor is modeled.

and arms are modeled as an ellipse and circles, respectively. The sizes of the torso and arms are included in the figure. This model is a two-dimensional version of the Thalmann model [11], which is a global numerical model of a walking human that includes a wide range of walking patterns and physiques. The model is widely used for numerical simulations of a human body [12].

Figure 2 shows a scenario in which a person walks along a narrow passage. The x–y coordinate system has its origin at interferometer 1, and x and y are in the horizontal and vertical directions in the figure. Interferometer 2 is 4.0 m apart from the interferometer 1, and both interferometers are on the center line between the walls. The person walks towards the bottom of the figure at an average speed of 1.32 m/s, with both arms swinging in a cycle lasting 1.41 s. The initial position of the torso at $t = 0$ is 0.3 m apart from the center line of the passage, and 3.2 m from the x-axis. The whole body moves uniformly at the same speed, while arms swing relatively to the torso. The torso rotates periodically while moving along a straight line, which is synchronized with the arm swings. The torso angle θ_t is modeled as a sinusoidal function $\theta_t(T) = \theta_{t0} \sin(\omega_h T)$, where T is a slow time, $\theta_{t0} = 10°$ and $\omega_h = 2\pi/1.41$ rad/s.

Figure 3 presents the walking human body model used in this study, with the outline of the torso and arms in black, the long axis of the torso in red, and the arms associated with the torso shown by blue dashed lines. This model describes a person walking towards the bottom of the figure. Interferometer 1 is shown as a black square at the origin.

Using two transmitters and four receivers, we construct two interferometers consisting of a transmitter and two receivers closely located. The two receivers in each pair are 5.0 mm apart in the x direction, corresponding to approximately half a wavelength, and the transmitter is located in the middle. The phase difference between the two receivers is detected to determine the DOA. We also exploit the multipath effect with a single reflection on a wall. In fact, there are many multipath propagation paths involving more than one reflection on a wall as discussed in Sect. 7.

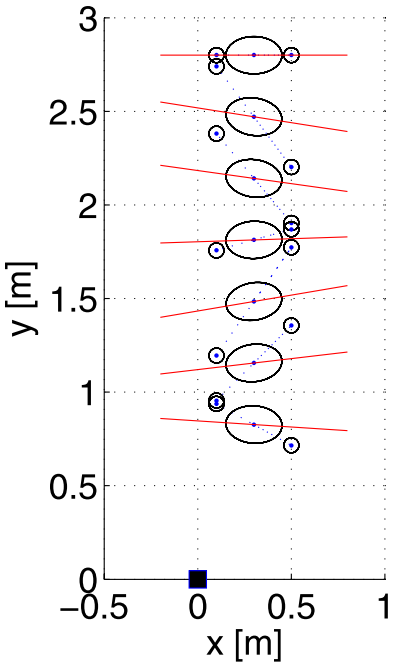

Fig. 3 Schematic of the walking human model (drawn every 250 ms), with the outlines of the torso and arms in black, the long axis of the torso in red, and the arms associated with the torso shown by blue dashed lines. Interferometer 1 is shown as a black square.

In our simulation, received signals are generated using the ray-tracing model detailed below. The simulation does not consider waveform distortion but considers the signal delay, phase shift, shadowing and attenuation depending on the radar cross-section (RCS) of the target and the propagation path length. The approximation is valid in this study because we assume a relatively narrow fractional bandwidth of 3%. The transmitted signal has a center frequency f_0, an-

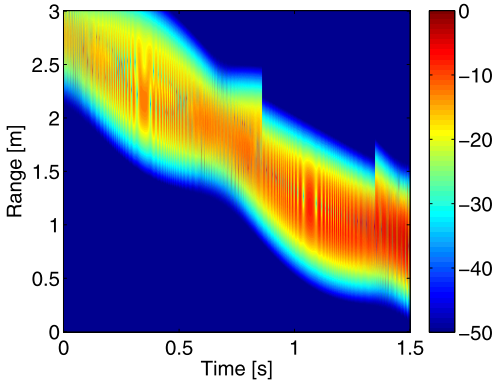

Fig. 4 Echoes from a walking person received using interferometer 1 (in dB).

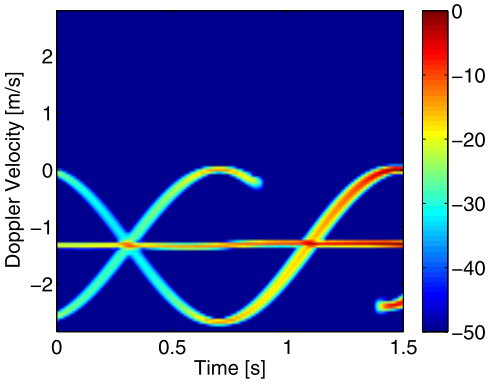

Fig. 5 Spectrogram calculated using the STFT from the echoes shown in Fig. 4 with a window width of 128 ms (in dB). Micro-Doppler components generated by the motion of arms are seen.

gular frequency $\omega_0 = 2\pi f_0$ and pulse envelope $p(t)$, where t is a fast time. The echo $s(t)$ from a single target after propagating distance l is then

$$s(t) = \alpha p(t - 2l/c)\mathrm{e}^{\mathrm{j}(\omega_0+\omega_\mathrm{d})(t-2l/c)}, \tag{1}$$

where α is the signal amplitude depending on the RCS and propagation path length, $p(t)\mathrm{e}^{\mathrm{j}\omega_0 t}$ is the transmitted waveform, and ω_d is the Doppler angular frequency calculated as $\omega_\mathrm{d} = 4\pi v_\mathrm{d} f_0/c$, with v_d being the radial speed of the target, and c is the speed of light. Considering a typical walking speed of 1.0 m/s, a microwave carrier of $f_0 = 26.4$ GHz, and a pulse width of 2.0 ns, we obtain $\omega_\mathrm{d} = 2\pi \times 176$ Hz, which is much smaller than $\omega_0 = 2\pi \times 26.4$ GHz considering the pulse width of 2 ns. Consequently, ω_d can be reasonably ignored without affecting the results. Note that the Doppler effect exploited in this paper is the phase shift over a pulse-to-pulse interval that is long enough to detect the phase shift.

The received signal from N targets can be expressed as

$$s(t) = \sum_{n=1}^{N} \alpha_n p(t - 2l_n/c)\mathrm{e}^{\mathrm{j}\omega_0(t-2l_n/c)}, \tag{2}$$

where α_n is the coefficient of the n-th echo, determined by the RCS of the n-th target and propagation path. In this paper, we employ a free-space approximation in calculating α_n. We simplify the shadowing effect by setting $\alpha_n = 0$ if the propagation path is blocked by an obstacle. Here, α_n and l_n are functions of a slow time T. In particular, the T-dependency of l_n is used to separate multiple targets. The received signal is denoted $s(T, t)$, explicitly showing the dependency on the slow time T. Figure 4 shows the simulated time-range signal received using one of the antennas of interferometer 1. The fast time t is displayed as a corresponding range $r = ct/2$. For $0.8\mathrm{s} < t < 1.4$ s, the left arm is masked by the shadowing effect, resulting in a signal with less interference fluctuation.

3. Doppler Interferometry and Imaging

UWB Doppler interferometry [9] separates multiple echoes in the frequency domain and estimates their positions using the phase difference of receivers. If different scattering centers have different radial speeds, they can be separated in a time-frequency analysis employing, for example, a short-time Fourier transform (STFT).

After applying the STFT to data $s_1(T, t)$ and $s_2(T, t)$ received by receivers 1 and 2, respectively, we obtain a spectrogram $S_k(T, \omega, t)$ $k \in \{1, 2\}$ as

$$S_k(T, \omega, t) = \int s_k(T', t)w(T' - T)\mathrm{e}^{\mathrm{j}\omega T'}\mathrm{d}T', \tag{3}$$

where $w(T)$ is a window function and specifically a Gaussian function in this study. Figure 5 shows the spectrogram obtained by applying the STFT to the signals shown in Fig. 4. We can observe three trajectories corresponding to the torso and arms. The simulation takes into account shadowing effects, and thus part of the signal is blocked depending on the relative position of the targets and antennas. For $0.8\,\mathrm{s} < t < 1.4\,\mathrm{s}$, the left arm is blocked and invisible.

Next, we detect the dominant time-frequency peak points (T_i, ω_i, t_i) $(i = 1, \cdots, I)$ for each T that satisfies

$$\begin{aligned} \partial\left|S_k(T,\omega,t)\right|^2/\partial\omega\big|_{T=T_i,\omega=\omega_i,t=t_i} &= 0, \\ \partial\left|S_k(T,\omega,t)\right|^2/\partial t\big|_{T=T_i,\omega=\omega_i,t=t_i} &= 0 \end{aligned} \tag{4}$$

and

$$\begin{aligned} \partial^2\left|S_k(T,\omega,t)\right|^2/\partial\omega^2\big|_{T=T_i,\omega=\omega_i,t=t_i} &< 0, \\ \partial^2\left|S_k(T,\omega,t)\right|^2/\partial t^2\big|_{T=T_i,\omega=\omega_i,t=t_i} &< 0 \end{aligned} \tag{5}$$

with values greater than the threshold

$$|S_k(T_i, \omega_i, t_i)| > \theta_\mathrm{S} \max_{\omega} |S_k(T_i, \omega, t_i)|, \tag{6}$$

where the threshold is proportional to the maximum norm of the spectrogram for $T = T_i$ and $t_i = t_i$. From the phase difference $\Delta\phi_i = \angle S_1(T_i, \omega_i, t_i) - \angle S_2(T_i, \omega_i, t_i)$, we can estimate the DOA as

$$\theta_i = \sin^{-1}\left(\frac{\Delta\phi_i}{2\pi d/\lambda}\right), \tag{7}$$

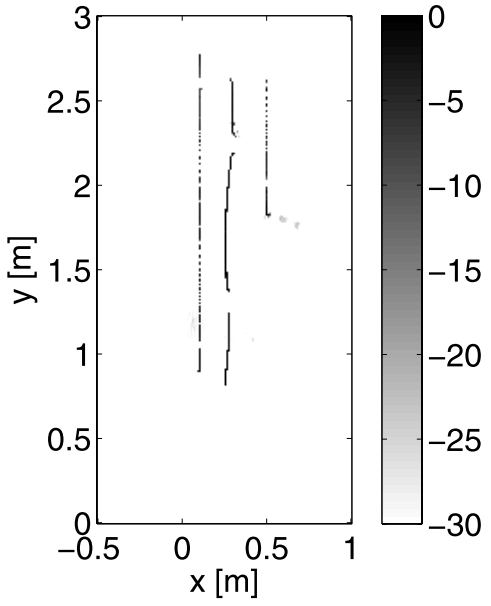

Fig. 6 The image estimated using interferometer 1 and Doppler interferometry (in dB).

where λ is the wavelength of the center frequency. This DOA estimation is correctly performed only if two targets are either located at different range gates, or moving at different radial speeds. Because we know the target range $r_i = ct_i/2$, we can estimate the target's position $\boldsymbol{x}_i$ by combining the range r_i and angle θ_i.

Figure 6 shows the image estimated using interferometer 1 with the Doppler interferometry from the time–frequency data in Fig. 5. The image was generated by superposing multiple image snapshots obtained at different slow times T over 1.5 s. It is seen that there are three trajectories, although they are partially blocked by other targets. This image alone, however, does not show the actual target shape, which will be tackled in the following part of this paper. The main idea is the use of multiple actual/virtual antennas available in a multipath environment, which can mitigate the shadowing effect and allow the estimation of the target velocity vector instead of the radial speed.

The method explained above can be applied to each of the propagation paths, leading to multiple sets of image points $\boldsymbol{x}_i^m$ for the m-th path ($m = 1, \cdots, M$). In our simulation, we assume $M = 6$, corresponding to two paths without any reflection on a wall and four paths with a single reflection on a wall. Note that each point $\boldsymbol{x}_i^m$ is labeled with a radial speed v_i^m that can be used to identify image points belonging to the same target, but measured by different paths.

Let $\boldsymbol{v}$ be the actual velocity vector of the target, and $\boldsymbol{i}_{i_1}^{m_1}$ and $\boldsymbol{i}_{i_2}^{m_2}$ be the unit radial vectors from the m_j-th path to the i_j-th image point for $j = 1$ and 2, respectively. The equations

$$\begin{cases} \boldsymbol{v}^{\mathrm{T}}\boldsymbol{i}_{i_1}^{m_1} &= v_{i_1}^{m_1} \quad \text{and} \\ \boldsymbol{v}^{\mathrm{T}}\boldsymbol{i}_{i_2}^{m_2} &= v_{i_2}^{m_2} \end{cases} \tag{8}$$

then hold, where $\cdot^{\mathrm{T}}$ is the transpose operator. These simultaneous equations have a solution except when $\boldsymbol{i}_{i_1}^{m_1}$ and $\boldsymbol{i}_{i_2}^{m_2}$ are parallel. To perform this calculation, however, the image points i_1 and i_2 must be correctly associated. If the wrong pair of points is chosen, the resultant velocity $\boldsymbol{v}$ is incorrect. When there are multiple echoes from the targets, their corresponding radial speeds differ and depend on the actual target position and velocity.

To avoid incorrect estimation of the target velocity, we can add one more condition, using three interferometers in total to ensure the simultaneous equations have a solution [13], [14]. We thus have

$$\begin{cases} \boldsymbol{v}^{\mathrm{T}}\boldsymbol{i}_{i_1}^{m_1} &= v_{i_1}^{m_1}, \\ \boldsymbol{v}^{\mathrm{T}}\boldsymbol{i}_{i_2}^{m_2} &= v_{i_2}^{m_2}, \\ \boldsymbol{v}^{\mathrm{T}}\boldsymbol{i}_{i_3}^{m_3} &= v_{i_3}^{m_3}. \end{cases} \tag{9}$$

This process suggests that redundancy in the number of interferometers is necessary to avoid erroneous association of echoes from different targets. In a multipath environment, the number of actual and virtual antennas becomes large, and thus, by exploiting the multipath effect, the same principle can achieve more stable estimation in associating echo pairs. This idea is discussed in detail in the following section.

4. Proposed Association Algorithm of Echoes Using the Radial Speed

In our system model, we use up to $M = 6$ propagation paths, corresponding to a ray-tracing simulation with a single wall-reflection. This allows us to obtain a stable solution for the antenna association problem stated in the previous section. However, we should note that not all the actual and virtual antennas can measure the same target, because of the shadowing effect. We propose a new method using a clustering algorithm in the velocity space to obtain the most likely combination of echoes that satisfy multiple simultaneous equations such as Eq. (9).

Let us assume that each of the six paths detects K echoes from the received signal. We then need to find likely combinations of echoes out of the ${}_M C_2 K^2$ combinations. The proposed method proceeds as follows. First, we calculate the simultaneous equations (Eq. (8)) for all ${}_M C_2 K^2$ combinations to obtain multiple radial speeds. These estimated velocities are displayed on a 2D velocity space (v_x, v_y). We then find clusters of velocity points that have high density, while leaving other points that are scattered less densely. In this way, we obtain multiple simultaneous equations that have the same solution that corresponds to the actual target velocity.

The k-means method, a well-known clustering algorithm, is not suited to this purpose because it assigns all data points to one of the resultant clusters [15]. However, our problem can be solved by finding a few dense clusters while rejecting false points generated by wrongly associated echoes.

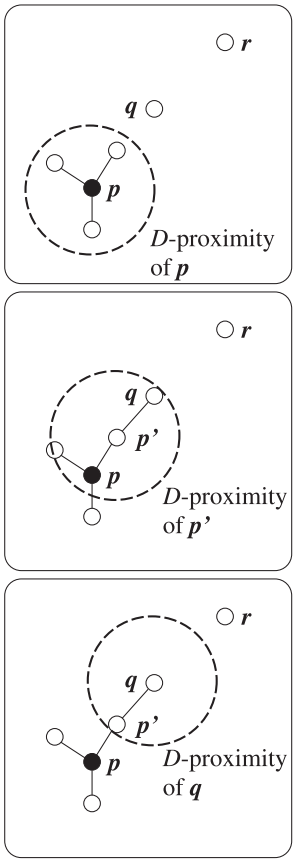

Fig. 7 Schematic of the DBSCAN algorithm. Within the D-proximity of $\boldsymbol{p}$, there are three nodes including $\boldsymbol{p}'$ (top). There is only one new node $\boldsymbol{q}$ within the D-proximity of $\boldsymbol{p}'$ (middle). However, $\boldsymbol{r}$ is not reachable from any nodes of the cluster (bottom).

Considering this unique aspect of our problem, we adopt the density-based spatial clustering of applications with noise (DBSCAN) [16]. DBSCAN not only separates given data points into multiple clusters but also rejects points that do not form any dense clusters. The actual procedure of DBSCAN is as follows. First, $\boldsymbol{p}$, one of the data points, is randomly selected. Next, $N(\boldsymbol{p})$, which is a set of points within D-proximity of $\boldsymbol{p}$, is calculated. Then, if $\boldsymbol{q}$ satisfies $\boldsymbol{q} \in N(\boldsymbol{p})$ and $|N(\boldsymbol{p})| \geq N_{\min}$, $\boldsymbol{q}$ is classified as a density-reachable point and included in the same cluster as $\boldsymbol{p}$. These steps are iteratively repeated until all the density-reachable points are included in the cluster.

Figure 7 is a schematic showing how DBSCAN works. In the figure, the point $\boldsymbol{p}$ is an element of a cluster, and we check if the other points $\boldsymbol{p}'$, $\boldsymbol{q}$, and $\boldsymbol{r}$ belong to the same cluster. The point $\boldsymbol{p}'$ is in the same cluster because it is within the D-proximity of $\boldsymbol{p}$. The point $\boldsymbol{q}$ is an element of the same cluster because it is density-reachable from $\boldsymbol{p}$ via another point $\boldsymbol{p}'$. In contrast, $\boldsymbol{r}$ does not belong to the same cluster because it is not density-reachable from any element of the cluster. In the figure, the D-proximity of $\boldsymbol{q}$ is shown in the image at the bottom. As a result, the point $\boldsymbol{r}$ is classified as a false image generated by a wrongly associated echo pair.

The DBSCAN algorithm is first run in 2D velocity space v_x–v_y and secondary clustering is then performed in 3D time–velocity space t–v_x–v_y. The former 2D clustering corresponds to solving the simultaneous equations at each time step independently of other time steps. The latter 3D clustering uses the continuity of the target velocity over a short period of time, which is based on the assumption that a human body does not change speed abruptly. Note that the 2D clustering can reduce the number of data points dramatically, and we can thus accelerate the more time-consuming 3D clustering using only a small number of data points. We detect a median point among the points in each resultant cluster. These points are given to the next step for tracking, which is detailed in the next section.

5. Tracking of Clustered Velocities

The clustering procedures are followed by implementation of a tracking algorithm using an α–β filter [17], [18] to associate the data points over time. Let $\boldsymbol{v}(\tau_n)$ be one of the estimated target velocities in the previous section, where τ_n is the n-th discretized slow time T, and $\Delta\tau$ is the slow-time interval of the discretized slow time. The α–β filter gives the smoothed velocity $\boldsymbol{v}_{\mathrm{s}}(\tau_n)$ as

$$\begin{aligned} \boldsymbol{v}_{\mathrm{s}}(\tau_n) &= \boldsymbol{v}_{\mathrm{p}}(\tau_n) + \alpha(\boldsymbol{v}(\tau_n) - \boldsymbol{v}_p(\tau_n)), \\ \boldsymbol{a}_{\mathrm{s}}(\tau_n) &= \boldsymbol{a}_{\mathrm{p}}(\tau_n) + \beta(\boldsymbol{v}(\tau_n) - \boldsymbol{v}_p(\tau_n))/\Delta\tau, \\ \boldsymbol{v}_{\mathrm{p}}(\tau_n) &= \boldsymbol{v}_{\mathrm{s}}(\tau_{n-1}) + \Delta\tau\boldsymbol{a}_{\mathrm{s}}(\tau_{n-1}), \\ \boldsymbol{a}_{\mathrm{p}}(\tau_n) &= \boldsymbol{a}_{\mathrm{s}}(\tau_{n-1}), \end{aligned} \tag{10}$$

where $\boldsymbol{v}_{\mathrm{p}}(\tau_n)$ is the predicted velocity, and $\boldsymbol{a}_{\mathrm{p}}(\tau_n)$ and $\boldsymbol{a}_{\mathrm{s}}(\tau_n)$ are the predicted and smoothed accelerations, respectively.

The selection of the points for tracking is determined as

$$|\boldsymbol{v}(\tau_n) - \boldsymbol{v}_{\mathrm{p}}(\tau_n)| \leq D_{\mathrm{v}}, \tag{11}$$

where D_{v} is a threshold value. If there are multiple points satisfying this condition, the nearest one is chosen. If there are no points satisfying this condition, $\boldsymbol{v}(\tau_n) = \boldsymbol{v}_{\mathrm{p}}(\tau_n)$ is assumed. After the tracking process, we compensate for the motion of each target to form an image corresponding to the initial position. Finally, we apply an artifact suppression algorithm [13] to remove artifacts from the image.

6. Performance Evaluation of the Proposed Method

The center frequency and bandwidth of the radar system are 26.4 GHz and 500 MHz, the antennas are omni-directional in the 2D plane assumed in this study, and the sampling frequency for slow time is 1.0 ms. The total observation time is 1.5 s, but we process the data below only for $0.4\,\mathrm{s} \leq t \leq 0.8\,\mathrm{s}$. The width of the window function $w(T)$ used for STFT is 128 ms, and the threshold is $\theta_{\mathrm{S}} = 0.005$. We set the parameters for the DBSCAN algorithm as $D = 0.1$ m/s, $N_{\min} = 5$, $D_{\mathrm{a}} = 0.4$ m/s, $D_{\mathrm{b}} = 0.1$ s, and $N'_{\min} = 80$, where D_{a} and D_{b} are the major and minor axes of an ellipsoid defining the proximity in the 3D t–v_x–v_y space. The signal-to-noise ratio

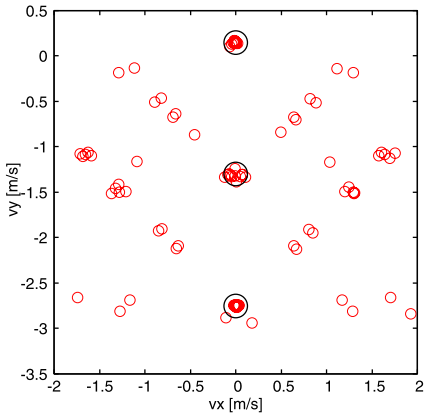

Fig. 8 Target velocities estimated from all possible combinations of paths. The actual target velocities are shown as black circles.

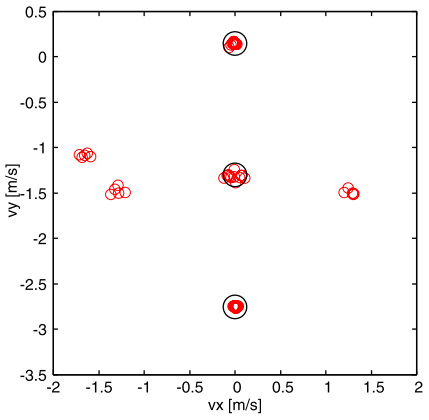

Fig. 9 Output of 2D DBSCAN clustering. Many of the false images are eliminated. The actual target velocities are shown as black circles.

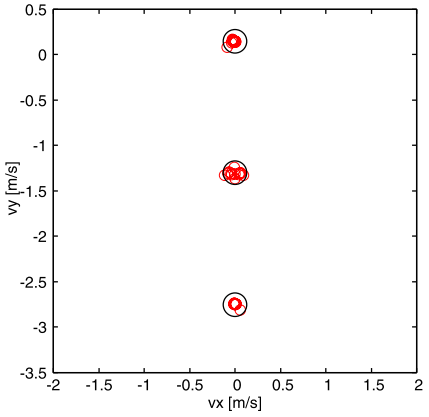

Fig. 10 Output of 3D DBSCAN clustering. Data points are estimated correctly. The actual target velocities are shown as black circles.

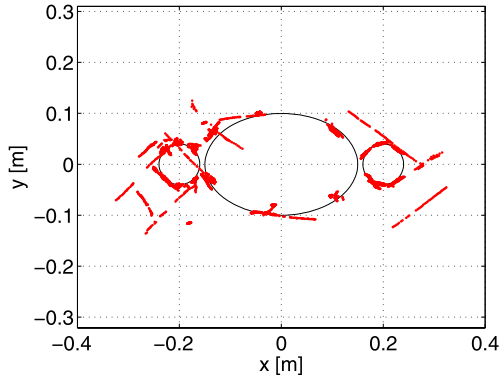

Fig. 11 Target image estimated without 3D clustering or artifact suppression (S/N=27.0 dB).

(S/N) is difficult to define because it varies over time, and depends on the antenna position and target shape. The average S/N is 27.0 dB, with the average being taken over the whole observation time, the 12 actual/virtual receivers and the three targets (torso and arms). Figure 8 shows the target velocities estimated by solving the simultaneous equation Eq. (8). We see there are numerous candidate points. In the figure, black circles are actual target velocities corresponding to the torso and arms.

After applying the DBSCAN algorithm in the 2D v_x–v_y space, we obtain the reduced data points shown in Fig. 9. Employing 2D DBSCAN, many of the data points are classified as artifacts. However, there are still unnecessary points included in the figure. Finally, we apply 3D DBSCAN in t–v_x–v_y space, exploiting the time continuity of the actual motion. The resultant data points are shown in Fig. 10. This example demonstrates that the proposed method can accurately estimate target velocities using the clustering approach. However, the instantaneous velocity estimated at each time sample is not sufficient to compensate for the target motion that includes acceleration. Therefore, we apply the α–β filter to the extracted clustered data points, and connect the associated data points over time, and thus estimate the motion of each target (the torso or one of the arms) that changes its velocity over time.

We now know the motion of the targets, and can thus compensate for the motion to back-propagate the estimated images to the initial position, and thus form an image. Figures 11 and 12 are respectively the target image estimated using the proposed method without the 3D DBSCAN algorithm or artifact suppression and with the 3D DBSCAN algorithm and artifact suppression. In the images, the estimated points are plotted in red, which are superposed with the actual target outline shown in black. These results show the importance of the information about the time continuity of the actual target motion. We note that the periodical rotation of the torso is not estimated or compensated for in our approach; only the translational motion is compensated for. Thus, the resultant image suffer from an error generated by the target rotation. In reality, however, the rotational angle of a torso is not important, and the image generated using the proposed method presents the target shape accurately enough in practice.

The root-mean-square (RMS) error in estimating the target shape is 5.2 mm, where the error ϵ_i is defined as the

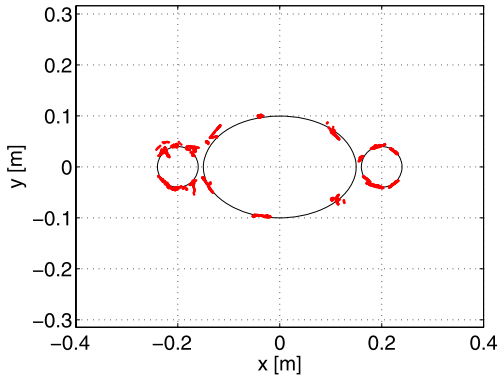

Fig. 12 Target image estimated using the proposed method (S/N=27.0 dB).

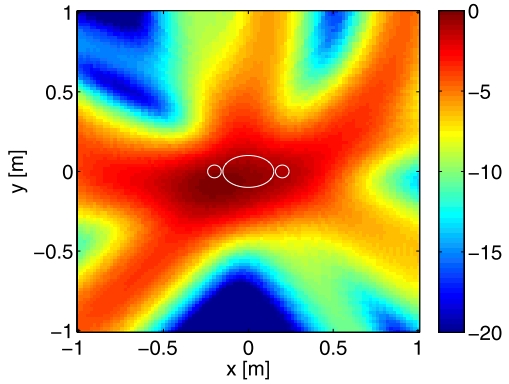

Fig. 13 Target image estimated using the DAS migration (in decibels). The actual target outline is shown in white.

distance between each image point $\boldsymbol{x}_i$ and the point on the target outline that is closest to the image point; i.e.,

$$\epsilon_i = \min_{\boldsymbol{q}} |\boldsymbol{x}_i - \boldsymbol{q}| \quad \text{subject to} \quad \boldsymbol{q} \in B, \tag{12}$$

where B is the boundary of the target shape including the torso and arms. The image coverage ratio of 30.2% is the percentage of the target outline covered by the group of estimated image points. The image shown in Fig. 12 clearly shows the outline of the 2D section of the human body, which demonstrates the effectiveness of the proposed method.

It should be noted that the image in Fig. 12 is not an image produced from a single snapshot signal measured at a particular time, but instead, is generated by combining multiple images produced using data snapshots over a certain period $0.4\,\text{s} \le t \le 0.8\,\text{s}$. We compensate for motions of the targets (torso and arms), estimated through clustering and tracking processes in the proposed method, to combine multiple snapshots to produce the image. For this reason, even the left arm is correctly imaged in Fig. 12, whereas part of the left arm trajectory is missing in Fig. 6 due to a shadowing effect.

For comparison, we apply a conventional delay-and-sum (DAS) migration to the same dataset processed above, to obtain the image shown in Fig. 13. The image is normalized to the maximum value (0 dB), and the actual target outline is shown in white. Because the DAS migration assumes that the target is stationary, the obtained image is calculated from a single data snapshot measured at $t = 0$. This method does not exploit Doppler information, but only the delay through six different propagation paths. Although the image shows approximate location of the set of targets, the resolution is not sufficient to resolve the target shape. This result demonstrates the effectiveness of the proposed method, which can estimate a clear target shape from limited data. This result is not possible with a conventional imaging methods.

Figure 14 shows the RMS error in imaging using the proposed method for various S/N values. The error is averaged over 50 realizations for each S/N value. When S/N is higher than 20 dB, the RMS error is below 10.0 mm, which is sufficiently accurate in practice to depict the outline of a human body.

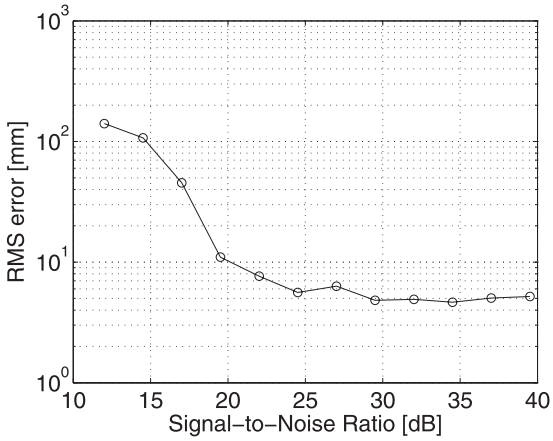

Fig. 14 RMS error in imaging using the proposed method.

7. Discussion

7.1 Human Model

In this study, we adopted the numerical human model introduced in Sect. 2 with a set of fixed parameters. Although this model exemplifies a typical walking human motion, there are numerous different walking patterns and body sizes. Therefore, it is imperative for future studies to assess the performance of the proposed method with various human motion and size parameters.

7.2 Multipath Model

Although we considered a multipath model only with a single wall reflection above, the actual signals contain multipath echoes involving more than one wall reflection. When assuming a multipath with R wall reflections, the total number of propagation paths is $M = 4R + 2$. This affects

the number of possible combinations of echoes ${}_MC_2K^2$ as stated in Sect. 4. Because the computational complexity of DBSCAN clustering C_{DBSCAN} is proportional to the number of possible combinations ${}_MC_2K^2$, this readily leads to $C_{\mathrm{DBSCAN}} \propto (4R+2)(4R+1) \sim O(R^2)$, where O denotes big O notation. This result indicates that the clustering process in the proposed method has order R^2 time complexity.

However, it should be noted that a multipath echo with a large R has a large delay, and can be suppressed by range-gating when using a UWB signal. Furthermore, because the signal intensity of a multipath echo decays exponentially for a large R, the number of multipath echoes to be processed is limited. For these reasons, we can prevent the computational complexity from increasing in practice. Nonetheless, it will be important to clarify the conditions required for application of the proposed method by considering the multipath environment and the computational complexity.

7.3 Waveform Model

A UWB signal is defined as a signal with a fractional bandwidth larger than 20% or a bandwidth wider than 500 MHz by the Federal Communications Commission. Although we assumed UWB pulse radar with a bandwidth of 500 MHz in the paper, as long as near-field ranging can be performed, any radar signals can be used equally as well. Possible candidates are impulse radio signals, wideband chirp signals, wideband FM-CW signals, and wideband code modulated signals.

The assumed bandwidth (500 MHz) corresponds to a range resolution of 30 cm, which is actually not high enough to resolve body parts (e.g., torso and limbs) of the same person. Therefore, separation of body parts is performed mainly using their different Doppler velocities. However, if the proposed method is applied to a scenario in which multiple people are present, the use of UWB signals remarkably simplifies signal processing, as simply applying range-gating suppresses echoes from other people.

8. Conclusion

We proposed a new UWB radar-imaging algorithm using two Doppler interferometers in a multi-path environment. The multipath effect provides redundant propagation paths, which allows detection of the most probable combination of echoes. We adopted a DBSCAN clustering algorithm to find densely clustered data points, leading to successful estimation of the target motion. The estimated target motion was compensated for to obtain the target image. The result indicates the effectiveness of the proposed method in imaging a realistic target model, simulating a walking person. An important future task is to apply the proposed method to measurement data for an actual human body to demonstrate the performance of the method.

Acknowledgment

We thank Dr. Kenshi Saho (Ritsumeikan University, Japan) for his help and advice. This research was partially supported by the Supporting Program for Interaction-based Initiative Team Studies, Center of Innovation Program, JSPS KAKENHI Grant Number 25249057 and 15K18077, and the R&D project for expansion of radio spectrum resources for more efficient use of frequency resources for the future supported by The Ministry of Internal Affairs and Communications, Japan.

References

[1] S. Nobuhara, Y. Tsuda, I. Ohama, and T. Matsuyama, "Multi-viewpoint silhouette extraction with 3D context-aware error detection, correction, and shadow suppression," IPSJ Trans. Comput. Vis. Appl., vol.1, pp.242–259, 2009.
[2] A. Mittal and L.S. Davis, "A general method for sensor planning in multi-sensor systems: Extension to random occlusion," Int. J. Comput. Vision., vol.76, no.1, pp.31–52, 2007.
[3] S. Kidera, T. Sakamoto, and T. Sato, "High-resolution and real-time three-dimensional imaging algorithm with envelopes of spheres for UWB radars," IEEE Trans. Geosci. Remote Sens., vol.46, no.11, pp.3503–3513, 2008.
[4] T.C. Williams, J.M. Sill, and E.C. Fear, "Breast surface estimation for radar-based breast imaging systems," IEEE Trans. Biomed. Eng., vol.55, no.6, pp.1678–1686, 2008.
[5] X. Zhuge and A.G. Yarovoy, "A sparse aperture MIMO-SAR-based UWB imaging system for concealed weapon detection," IEEE Trans. Geosci. Remote Sens., vol.49, no.1, pp.509–518, 2011.
[6] S. Bertl, A. Dallinger, and J. Detlefsen, "Interferometric focusing for the imaging of humans," IET Radar Sonar Navig., vol.4, no.3, pp.457–463, 2010.
[7] A. Lin and H. Ling, "Doppler and direction-of-arrival (DDOA) radar for multiple-mover sensing," IEEE Trans. Aerosp. Electron. Syst., vol.43, no.4, pp.1496–1509, 2007.
[8] A. Lin and H. Ling, "Frontal imaging of human using three- element Doppler and direction-of-arrival radar," Electron. Lett., vol.42, no.11, pp.660–661, 2006.
[9] K. Saho, T. Sakamoto, T. Sato, K. Inoue, and T. Fukuda, "Pedestrian imaging using UWB Doppler radar interferometry," IEICE Trans. Commun., vol.E96-B, no.2, pp.613–623, 2013.
[10] T. Sakamoto, Y. Matsuki, and T. Sato, "Method for the three-dimensional imaging of a moving target using an ultra-wideband radar with a small number of antennas," IEICE Trans. Commun., vol.E95-B, no.3, pp.972–979, 2012.
[11] R. Boulic, N.M. Thalmann, and D. Thalmann, "A global human walking model with real-time kinematic personification," The Visual Computer, vol.6, no.6, pp.344–358, 1990.
[12] P. van Dorp and F.C.A. Groen, "Human walking estimation with radar," IEE Proc., Radar Sonar Navig., vol.150, no.5, p.356, 2003.
[13] H. Yamazaki, K. Saho and T. Sato, "Accurate shape estimation method for multiple moving targets with UWB Doppler radar interferometers," Proc. International Conference on Space, Aeronautical and Navigational Electronics 2013, Dec. 2013.
[14] H. Yamazaki, T. Sakamoto and T. Sato, "Accurate two-dimensional imaging of a human body in motion using multiple ultra-wideband Doppler radar systems in a multipath environment," Proc. International Conference on Space, Aeronautical and Navigational Electronics 2014, Oct. 2014.
[15] J. MacQueen, "Some methods for classification and analysis of multivariate observations," Proc. Fifth Berkeley Symp. Math. Statist. Prob., vol.1, pp.281–297, 1967.

[16] M. Ester, H.-P. Kriegel, J. Sander, and X. Xu, "A density-based algorithm for discovering clusters in large spatial databases with noise," Proc. 2nd International Conference on Knowledge Discovery and Data Mining, 1996.
[17] Y. Kosuge, M. Ito, T. Okada, and S. Mano, "Steady-state errors of an α–β–γ filter for radar tracking," Electron. Comm. Jpn. Pt. III, vol.85, no.12, pp.65–79, 2002.
[18] Y. Kosuge and M. Ito, "A necessary and sufficient condition for the stability of an α–β–γ filter," Proc. 40th SICE Annual Conference, International Session Papers (IEEE Cat. No.01TH8603), pp.52–57, 2001.

Takuya Sakamoto received the B.E. degree in electrical engineering from Kyoto University, Kyoto, Japan, in 2000 and the M.I. and Ph.D. degrees in communications and computer engineering from the Graduate School of Informatics, Kyoto University, in 2002 and 2005, respectively. Since 2015, he has been an Associate Professor at the Graduate School of Engineering, University of Hyogo, and also a Researcher at the Graduate School of Informatics, Kyoto University. From 2006 through 2015, he was an Assistant Professor at the Graduate School of Informatics, Kyoto University. From 2011 through 2013, he was also a Visiting Researcher of Microwave Sensing, Signals and Systems, Delft University of Technology, Delft, the Netherlands. Dr. Sakamotob's current research interests are in ultra-wideband radar, radar imaging, and radar signal processing. He is a member of the Institute of Electrical and Electronics Engineers, the Institute of Electrical Engineers of Japan, and the Japan Society of Ultrasonics in Medicine.

Hiroki Yamazaki received his B.E. degree from Kyoto University, Kyoto, Japan, in 2013. He is currently working toward his M.S. degree at the Graduate School of Informatics, Kyoto University. His research interests include Doppler interferometry and ultra-wideband radar imaging.

Toru Sato received his B.E., M.E., and Ph.D. degrees in electrical engineering from Kyoto University, Kyoto, Japan, in 1976, 1978, and 1982, respectively. He has been with Kyoto University since 1983 and is currently a Professor at the Department of Communications and Computer Engineering, Graduate School of Informatics. His major research interests have been system design and signal processing aspects of atmospheric radars, radar remote sensing of the atmosphere, observations of precipitation using radar and satellite signals, radar observation of space debris, and signal processing for subsurface radar signals. Prof. Sato is a member of the Institute of Electronics, Information, and Communication Engineers of Japan, the Society of Geomagnetism and Earth, Planetary and Space Sciences, the Japan Society for Aeronautical and Space Sciences, the Institute of Electrical and Electronics Engineers, and the American Meteorological Society. He was awarded the Tanakadate Prize in 1986.